



Development of high B_s Fe–Ni-based metal amorphous nanocomposite by optimization of glass-forming ability

Y. Krimer^{1,a)}, A. Barberis¹, M. E. McHenry¹

¹Department of Materials Science, Carnegie Mellon University, Pittsburgh, PA, USA

^{a)}Address all correspondence to this author. e-mail: ykrimer@andrew.cmu.edu

Received: 21 January 2021; accepted: 19 March 2021; Published online: 5 April 2021

Thermocalc simulations identified compositions with good glass-forming ability (GFA) by locating minima in liquidus temperature, and solidification range in $(\text{Fe}_{70}\text{Ni}_{30})_x(\text{B-Si-Nb})_{100-x}$ alloys with $x = 82\%$ and $x = 85\%$, increased compared to previously developed $x = 80\%$ alloys. 3 compositions in the $x = 82\%$ system and 1 in the $x = 85\%$ system were successfully cast as amorphous magnetic ribbon. Magnetic properties of as-cast alloys showed improvements in Curie temperature and saturation induction, especially for the 85% alloy. Crystallization behavior in the 85% alloy was determined to occur as a 2-step process. Annealing studies showed $(\text{Fe}_{70}\text{Ni}_{30})_{82}\text{Nb}_2\text{Si}_0\text{B}_{16}$ and $(\text{Fe}_{70}\text{Ni}_{30})_{82}\text{Nb}_3\text{Si}_0\text{B}_{15}$ alloys to exhibit low coercivity and high B_s with annealing. TEM results show significant crystallization in as-cast ribbon. The $(\text{Fe}_{70}\text{Ni}_{30})_{85}\text{Nb}_{0.5}\text{Si}_0\text{B}_{14.5}$ alloy as-cast has small, uniformly distributed grains, allowing a useful nanocrystalline alloy to be produced as cast. Finally, the parameter ΔT_{xg} , the temperature range in which the material can be thermomechanically processed, was in the range of 12–23 °C.

Introduction

An estimate by the International Energy agency puts the electrical consumption by electric motors at ~46% of the world total, accounting for 6040 MT of CO₂ emissions [1]. As such, improving the efficiency of electric motors is a high priority. Iron losses, or losses within the magnetic core, which include eddy current and hysteresis losses, account for a significant portion of the total losses in a magnetic component, so reducing these losses is the subject of much effort [2].

Increased use of electric motors in vehicle applications demands improvements in power density as well as efficiency compared to existing motor designs. One way of improving power density is by using amorphous magnetic ribbon (AMR) or metal amorphous nanocomposite (MANC) materials, which allows higher switching frequencies. Since motor power density scales with speed, improved switching frequencies allow power density to be increased. These materials have very low coercivity, which reduces hysteresis losses, and the presence of a residual amorphous phase reduces eddy current losses by increasing electrical resistivity. Additionally, the thin nature of these materials, which are typically produced as 15–25 μm ribbons, further reduces eddy current losses. The losses in a magnetic material are given by the Steinmetz equation [3]:

$$P_L = kf^\alpha B^\beta = A_{\text{Hyst}}f(\text{hysteresis}) + \frac{d^2 B^2 f^2}{\rho} (\text{eddy current}) + \frac{df^x}{\rho} (\text{anomalous}), \quad (1)$$

where P_L is core loss; k , α , and β are fitting parameters [3, 4]. A_{Hyst} is the area of the B – H loop, d is material thickness, and ρ is electrical resistivity. Hysteresis loss increases linearly with frequency. Classical eddy current loss scales as the square of the frequency, so in higher frequency applications, low eddy current loss becomes increasingly important.

Unfortunately, all commercial and experimental MANCs produced until now have shortcomings that prevent their use in electric motor applications. Fe-based MANCs, known commercially as FINEMET, have excellent magnetic properties but are extremely brittle, making them unsuitable for high-speed motors [5]. Fe-Co-based materials, known as HITPERM, have very high saturation inductions (B_s) and Curie temperatures, but high magnetostriction coefficients contribute to high hysteresis losses and magnetostrictive noise [6]. Co-based alloys have low losses and good mechanical properties, but saturation induction is limited to ~1 T [7, 8] and alloy components are expensive [9, 10]. Recently developed Fe–Ni-based MANCs show excellent magnetic softness, high Curie temperature, and improved

mechanical properties. Saturation inductions remain limited to ~ 1.2 T [3, 11].

Several studies have explored using MANCs for electric motors. Silveyra et al. [12, 13] simulated and built motors using Co-based MANCs, which showed significant reduction in size and power loss. Simizu et al. [11] demonstrated a flux switching motor using the newer Fe–Ni-based MANC, demonstrating high power density and low loss. However, all of these designs could be further improved in power density with increased saturation induction of the material. These motors are hybrid motors which also include permanent magnets in the stators. Both rare-earth-free and rare-earth-lean permanent magnets are being considered to improve power densities without use of the most expensive rare-earth magnets or rare-earth magnets at all.

One factor limiting saturation induction in MANCs is the necessity of glass formers, since these materials are initially produced by rapid solidification, and sufficient glass-forming ability (GFA) is necessary to form the amorphous precursor. Glass formers degrade magnetic performance by reducing content of magnetic elements. Recent studies have explored improving B_s by increasing the percentage of magnetic elements. It was noted that additions of P [14, 15], P and C [16–19], and other alloying additions [20] allowed the total percentage of magnetic elements to be increased in Fe-based alloys to as high as 85%, resulting in significant increases in B_s , without loss of GFA. However, no such work has been done on the Fe–Ni-based MANCs.

The proportions of the glass-forming elements are often chosen by trial and error, and optimization of glass former composition may allow increase in magnetic element content. Systematic studies of glass former variations have been made in FeCo-based metallic glasses where reduced metalloids glass former content was shown to increase magnetic inductions [19]. Similar studies on reduced early transition metals [20] showed similar results. It has been noted early in the history of amorphous alloy development that alloys with minima in liquidus temperatures have better GFA, especially eutectic or near eutectic compositions. Thermodynamic calculations have been performed previously to identify compositions with minima in liquidus temperatures in a given composition range [21–23], but these calculations are complex to perform. Zhang et al. [24] have used Thermocalc software to calculate liquidus temperature for bulk metallic glass alloys over a 3 component space and identified minima in liquidus temperature. This study additionally calculated the solidification range, which is defined as the difference between solidus and liquidus temperatures, and alloys showing minima in both liquidus temperature and solidification range were identified as having good GFA. Recently, Krimer et al. [25] have further explored the use of Thermocalc software to locate near eutectic compositions with maximum GFA in a given soft magnetic glass-forming system. Simulations were also conducted on alloy systems with 82% and 85% magnetic elements. It was noted

that this resulted in a significant shrinkage in regions with good GFA, though both systems had a composition range in which good GFA was expected. In this study, alloys in these composition ranges will be explored.

In addition to good GFA being necessary to produce an amorphous material, higher GFA is correlated to a higher value of the parameter $\Delta T_{xg} = T_x - T_g$ [26], which is necessary for thermomechanical forming and hot stamping of the material. Below T_g , the material is incapable of homogeneous deformation, while above T_x , the material crystallizes into a brittle nanocrystalline structure. Within that temperature range, the material is capable of viscous flow with very large strains [27, 28]. Maintaining good GFA will result in a high ΔT_{xg} value that will allow reduced die wear in stamping the many layers necessary for a motor core. The thin nature of the amorphous ribbon, as well as its extreme hardness, currently prevent large-scale manufacturing of MANC-based motors, since potentially thousands of layers need to be cut and stacked, resulting in excessive tool wear [29]. Prototype MANC-based motors have been successfully built, however [12, 30, 31]. Silveyra et al. [12] cut the individual layers by laser cutting, but large-scale production will use stamping, requiring enhanced formability. Die wear in stamping processes promises to provide less wear if an amorphous material with good GFA can be softened prior to the stamping operation. In reducing the amount of the growth inhibitor glass formers, one must be cognizant of their role in inhibiting grain growth [32] and providing virtual bound states which increase electrical resistivity. [33]

In summary, some current MANC materials have good mechanical properties, low losses, or high saturation inductions, but not all three. Successful implementation in electric motor applications will require a combination of these properties. Additionally, a sufficiently large ΔT_{xg} value will be necessary to allow stamping and thermomechanical forming of motor laminations. The aim of this work is to develop a material possessing all of these properties.

Results

Figure 1a and b shows the results of the Thermocalc simulation for the $x = 82\%$ alloy system, with dots showing alloys that were produced. A region with a clear minimum in liquidus is seen at 15–17% B and 0–5% Si. The corresponding minimum in solidification range is small, as seen in Fig. 2b. The 3 compositions were all successfully cast as continuous ribbon. Figure 1c and d shows Thermocalc results for the $x = 85\%$ alloy. As seen in the figure, the region with a minimum in both liquidus and solidification range is small. Nevertheless, a single alloy was successfully cast and confirmed to be amorphous by a bend test. All ribbons were determined to be 18–20 μm thick. The ribbons were confirmed to be mostly amorphous, with XRD results showing a broad

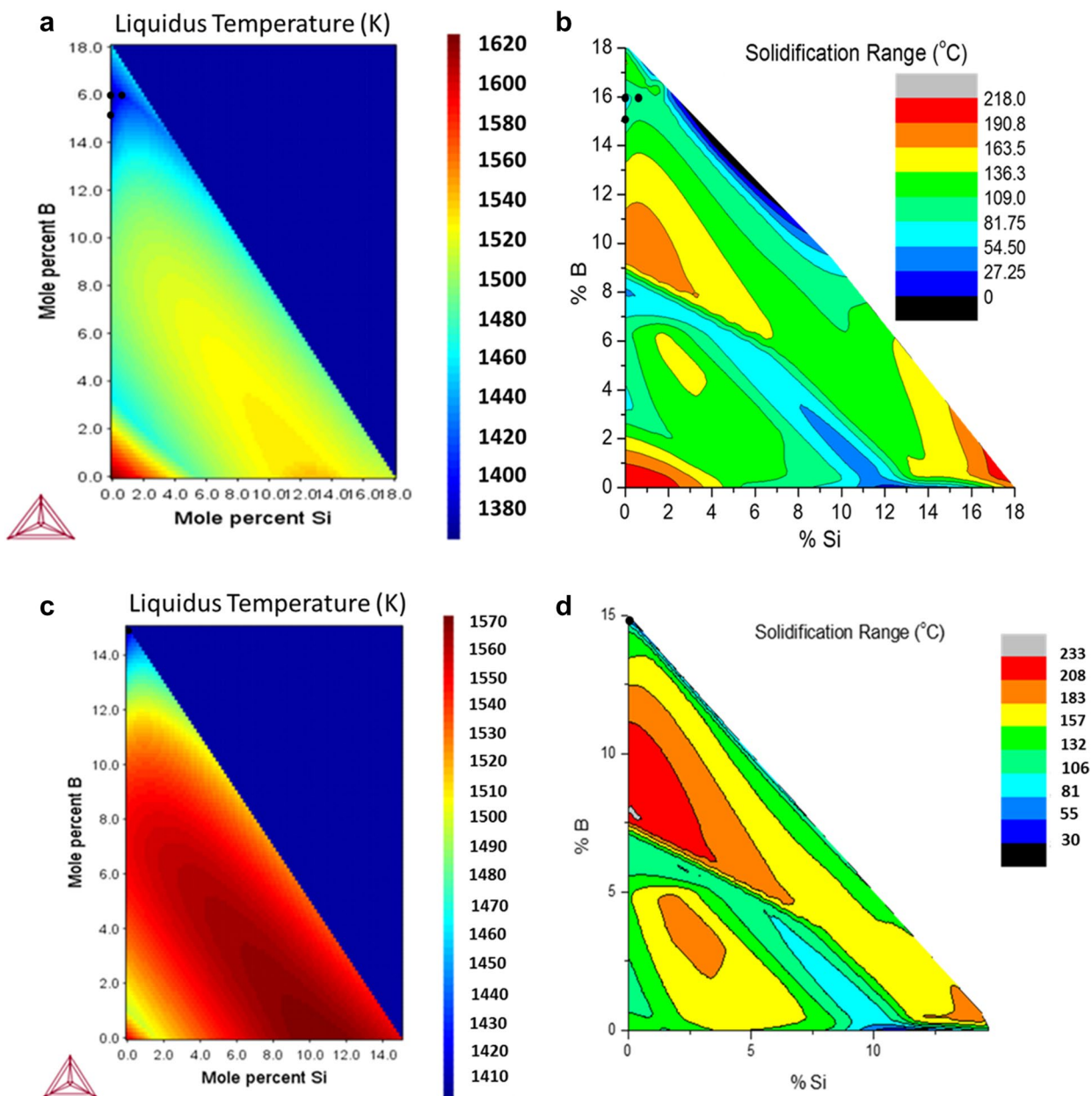


Figure 1: (a) Liquidus temperature and (b) solidification range of the $x=82\%$ alloys. (c) Liquidus temperature and (d) solidification range of the $x=85\%$ alloys.

amorphous peak (Fig. 2). However, all samples showed some evidence of crystallinity, especially in the case of the 85% alloy. This corresponds with the low expected glass-forming ability of this composition.

Magnetic properties are summarized in Table 1. Curie temperatures of the amorphous phase were in the range of 407–438 °C for the $x=82\%$ alloys and 462 °C for the $x=85\%$ alloy, showing improvement with increasing magnetic element content. Saturation induction of the as-cast samples was 1.28–1.36 T for the $x=82\%$ alloys, and 1.48 T for the $x=85\%$

alloys. The saturation induction of the $x=85\%$ alloy shows an especially promising improvement over the previously developed alloy and can be expected to further increase with crystallization. Coercivity of all samples was in the range of 25–40 A/m.

The magnetization vs. temperature curve of the $x=85\%$ alloy is shown in Fig. 3. The magnetization initially declines with temperature, as the Curie temperature of the amorphous phase is approached and then increases with crystallization. The increase was very sharp, occurring within one increment of the measurement.

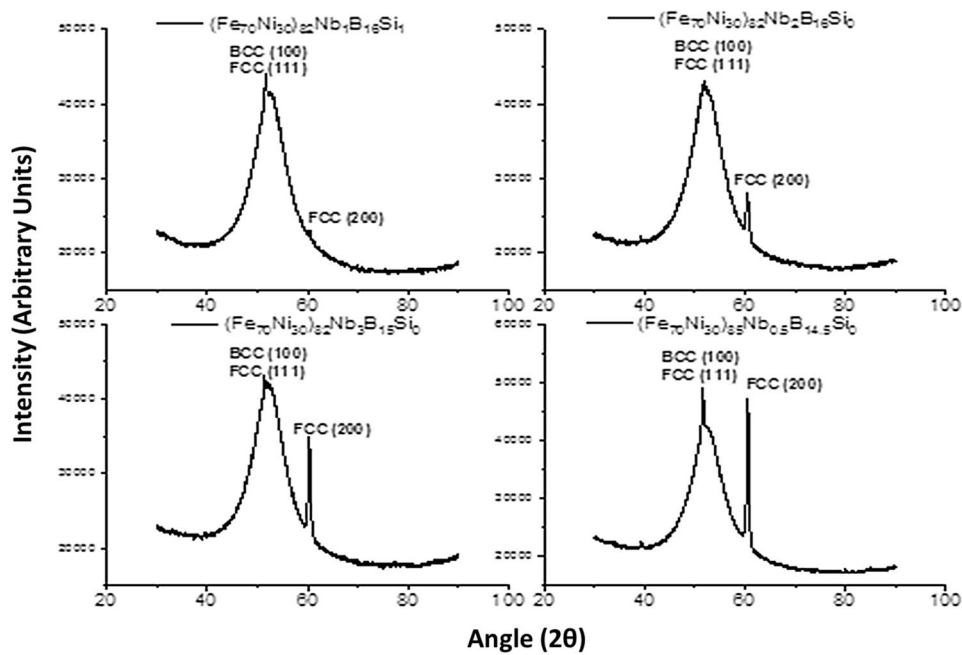
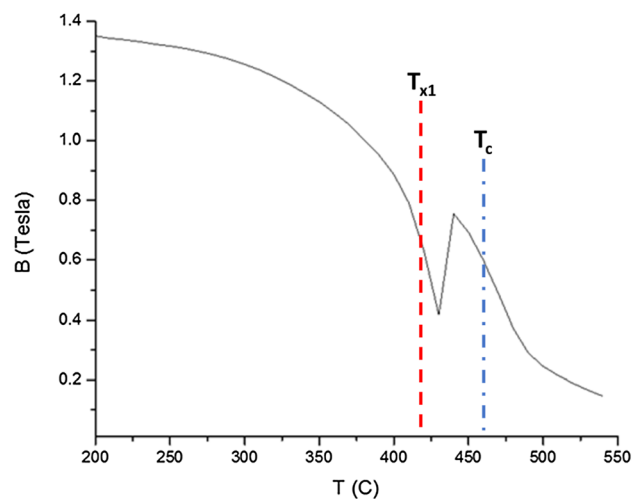


Figure 2: XRD results of the as-cast samples, showing a mostly amorphous structure with some crystallinity present, especially for the 85% alloy.

TABLE 1: Curie temperature, saturation induction, and coercivity of the as-cast alloys.

	$(\text{Fe}_{70}\text{Ni}_{30})_{82}\text{Nb}_{15}\text{Si}_{6}$ $_{0}\text{Nb}_{3}$	$(\text{Fe}_{70}\text{Ni}_{30})_{82}\text{Nb}_{16}\text{Si}_{6}$ $_{0}\text{Nb}_{2}$	$(\text{Fe}_{70}\text{Ni}_{30})_{82}\text{Nb}_{16}\text{Si}_{6}$ $_{1}\text{Nb}_{1}$	$(\text{Fe}_{70}\text{Ni}_{30})_{85}\text{Nb}_{0.5}\text{Si}_{6}$
$T_{c(\text{amorphous})}$ (°C)	407	417	438	462
B (Tesla)	1.32	1.36	1.28	1.48
H_c (A/m)	37.6	30.0	30.7	26.0

Figure 3: M vs. T curve ($x=85\%$ alloy) showing rapid magnetization increase with crystallization.



To the crystallization process, as well as the optimal annealing temperature, XRD was performed on samples annealed at temperatures of 415–445 °C. The results are shown in Fig. 4a. The material was shown to undergo a 2-step crystallization

process, with a BCC + FCC phase first appearing, followed by more complex phases at higher temperatures. Based on these results, an annealing temperature of 415 °C was chosen for optimal magnetic properties.

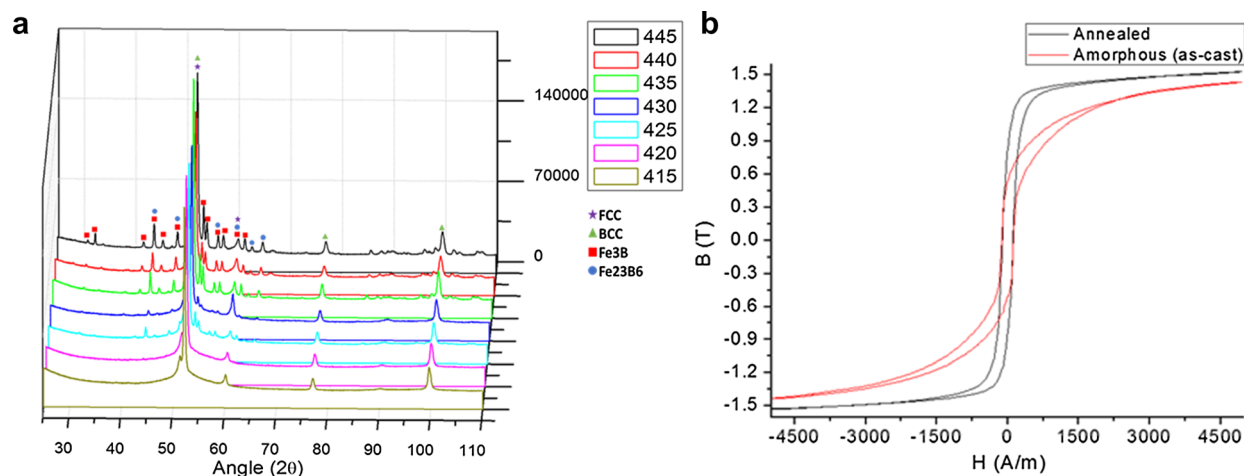


Figure 4: (a) XRD results of the $x=85\%$ alloy annealed at increasing temperatures, showing a 2-step crystallization process. (b) Strip testing result of the as-cast and annealed 3.5 mm ribbon.

TABLE 2: Glass transition and primary crystallization temperatures and supercooled liquid range for the tested alloys.

	$(\text{Fe}_{70}\text{Ni}_{30})_{0.82}\text{B}_{15}\text{Si}_3\text{Nb}_3$	$(\text{Fe}_{70}\text{Ni}_{30})_{0.82}\text{B}_{16}\text{Si}_0\text{Nb}_2$	$(\text{Fe}_{70}\text{Ni}_{30})_{0.82}\text{B}_{16}\text{Si}_1\text{Nb}_1$	$(\text{Fe}_{70}\text{Ni}_{30})_{0.85}\text{B}_{14.5}\text{Nb}_{0.5}\text{Si}_0$
T_g (°C)	420	431	421	399
T_{x1} (°C)	438	443	444	419
ΔT_{xg} (°C)	18	12	23	20

Figure 4b shows the strip-testing results of the annealed and as-cast ribbon of this alloy. Saturation induction of the as-cast alloy increased from 1.43 T for the as-cast to 1.53 T for the annealed sample. Additionally, the B–H loop became squarer. However, coercivity increased to 114 A/m, which is high for a nanocrystalline material.

Glass transition temperatures, primary crystallization temperatures, and ΔT_{xg} values are listed in Table 2. ΔT_{xg} ranges from 12 to 23 °C for the 82% alloys. For the $x=85\%$ alloy, the temperature range is 20 °C, which should be sufficient to allow hot stamping.

Annealing Results

The coercivity results are shown in Fig. 5. The onset of crystallization line marks where the hysteresis loops become squarer as crystallization begins. Coercivity of the $(\text{Fe}_{70}\text{Ni}_{30})_{0.82}\text{Nb}_1\text{Si}_1\text{B}_{16}$ alloy increases continuously with annealing, which is typical for alloys with low Nb content due to excessive grain coarsening. $(\text{Fe}_{70}\text{Ni}_{30})_{0.82}\text{Nb}_2\text{Si}_0\text{B}_{16}$ and $(\text{Fe}_{70}\text{Ni}_{30})_{0.82}\text{Nb}_3\text{Si}_0\text{B}_{15}$ both show a strong dip in coercivity with annealing above the crystallization temperatures, with the coercivity of both dropping to 16–17 A/m. The $(\text{Fe}_{70}\text{Ni}_{30})_{0.85}\text{Nb}_{0.5}\text{Si}_0\text{B}_{14.5}$ alloy has a sharp increase in

coercivity followed by a small drop upon crystallization, but coercivity remains excessive.

Figure 6 shows the saturation induction change with annealing. The alloys all experienced a drop in saturation induction with crystallization, which is unusual. This can be explained by the presence of crystallization in the as-cast samples, which means that they do not start out fully amorphous.

TEM Results

Figure 7 shows TEM results for the 4 as-cast alloys. $(\text{Fe}_{70}\text{Ni}_{30})_{0.82}\text{Nb}_1\text{Si}_1\text{B}_{16}$ was the only alloy that was mostly amorphous, as seen from the broad amorphous halo in the SADP. Both $(\text{Fe}_{70}\text{Ni}_{30})_{0.82}\text{Nb}_2\text{Si}_0\text{B}_{16}$ and $(\text{Fe}_{70}\text{Ni}_{30})_{0.82}\text{Nb}_3\text{Si}_0\text{B}_{15}$ showed larger crystalline grains more widely distributed in an amorphous matrix. Diffraction patterns show rings emerging, though the structure is largely amorphous. $(\text{Fe}_{70}\text{Ni}_{30})_{0.85}\text{Nb}_{0.5}\text{Si}_0\text{B}_{14.5}$ had a nearly ideal structure with evenly distributed, sub 10 nm grains with a clear residual amorphous matrix. The diffraction pattern shows more strongly defined rings with a mainly FCC structure. With only 15% glass-forming elements, $(\text{Fe}_{70}\text{Ni}_{30})_{0.82}\text{Nb}_4\text{Si}_2\text{B}_{14}$ had the lowest GFA of the 4 alloys and, therefore, exhibited the largest degree of crystallization.

Both $(\text{Fe}_{70}\text{Ni}_{30})_{0.82}\text{Nb}_2\text{Si}_0\text{B}_{16}$ and $(\text{Fe}_{70}\text{Ni}_{30})_{0.82}\text{Nb}_3\text{Si}_0\text{B}_{15}$ as-cast material were seen to have a bimodal grain size distribution. In the thin part of the TEM specimens, the grain size was small, at 5–20 nm. In the thicker parts of the specimens, some larger grains began to appear. A sharp transition between the regions with larger grain present and those with only small grains was seen. These regions are near the limit of electron transparency thickness and were very difficult to image.

Figure 8 shows TEM results for the annealed samples from the 4 alloys. $(\text{Fe}_{70}\text{Ni}_{30})_{0.82}\text{Nb}_1\text{Si}_1\text{B}_{16}$ had sporadically distributed grains with large size up to 50 nm. Ideal grain

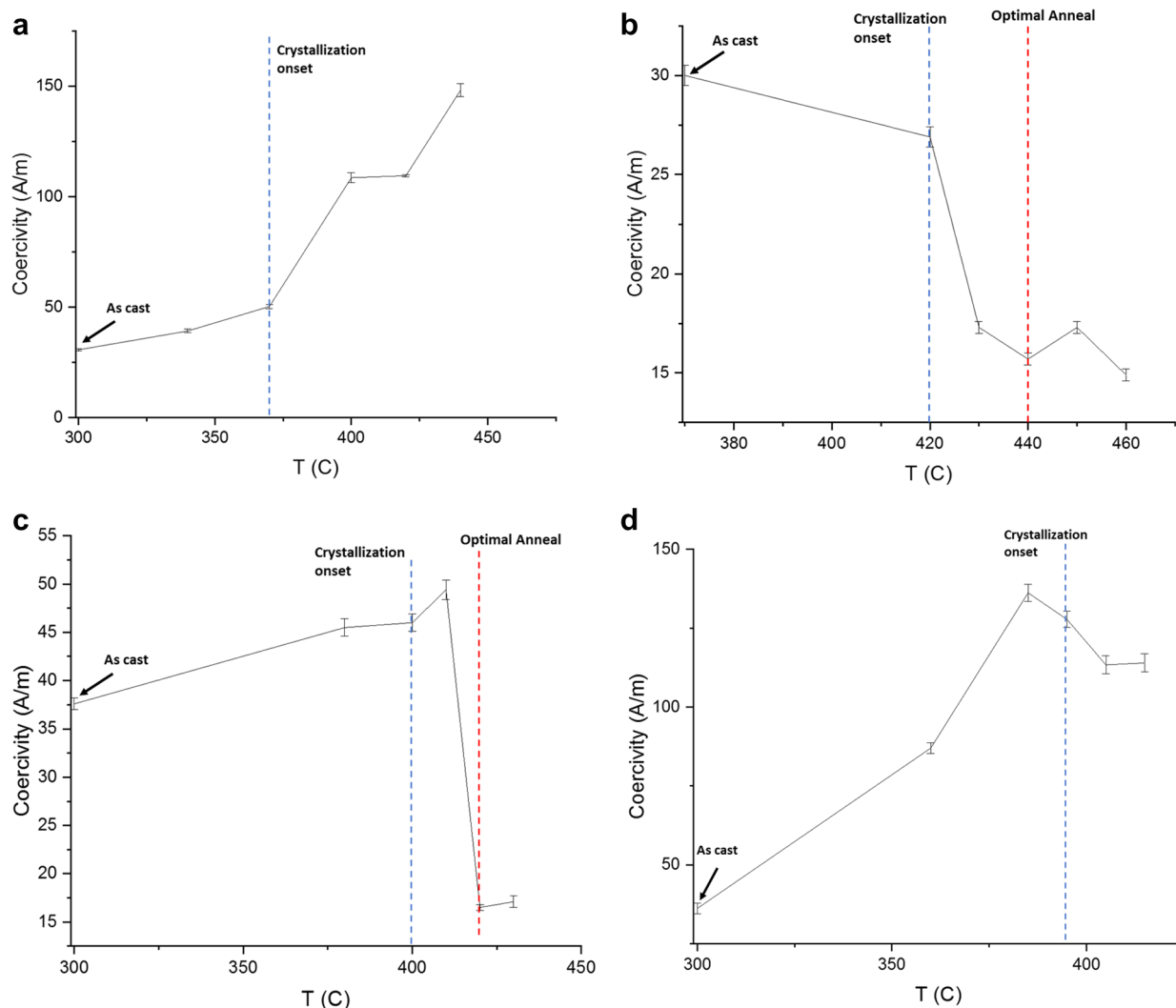


Figure 5: Coercivity of (a) $(\text{Fe}_{70}\text{Ni}_{30})_{82}\text{Nb}_1\text{Si}_1\text{B}_{16}$, (b) $(\text{Fe}_{70}\text{Ni}_{30})_{82}\text{Nb}_2\text{Si}_0\text{B}_{16}$, (c) $(\text{Fe}_{70}\text{Ni}_{30})_{82}\text{Nb}_3\text{Si}_0\text{B}_{15}$, and (d) $(\text{Fe}_{70}\text{Ni}_{30})_{85}\text{Nb}_{0.5}\text{Si}_0\text{B}_{14.5}$ alloys vs. annealing temperature.

size for MANC alloys is < 20 nm. Grains larger than the optimal size will result in high coercivity. $(\text{Fe}_{70}\text{Ni}_{30})_{82}\text{Nb}_2\text{Si}_0\text{B}_{16}$ and $(\text{Fe}_{70}\text{Ni}_{30})_{82}\text{Nb}_3\text{Si}_0\text{B}_{15}$ showed grains in the optimal sub 20 nm size range. The $(\text{Fe}_{70}\text{Ni}_{30})_{82}\text{Nb}_2\text{Si}_0\text{B}_{16}$ alloy had more sporadically distributed grains, while $(\text{Fe}_{70}\text{Ni}_{30})_{82}\text{Nb}_3\text{Si}_0\text{B}_{15}$ had uniform grains with a clear residual amorphous matrix. Both these alloys had low coercivity of 16–17 A/m, likely owing to the small grain size. It should be noted that the coarse grains seen in some areas of these alloys in the as-cast state are no longer seen. The reason for the disappearance of these large grains is unknown. The $(\text{Fe}_{70}\text{Ni}_{30})_{85}\text{Nb}_{0.5}\text{Si}_0\text{B}_{14.5}$ alloy had the largest grain size at over 100 nm for some grains. All samples show primarily a mixture of BCC and FCC patterns, and a residual amorphous halo.

Discussion

Thermocalc results for both the 82% and 85% alloy systems show minima in liquidus temperature, though this minimum becomes smaller with increasing magnetic elements from 82 to 85%. The minimum in solidification range is very small for the 82% system and nearly nonexistent for the 85% system. Therefore, GFA was not expected to be especially good but still sufficient to form amorphous ribbon. The minima occurred in the highest B composition region, so these compositions were chosen for experimental alloys.

Measurement of magnetic properties of the as-cast alloys shows significant improvement in both T_c and B_s compared to the previously developed 80% alloy, which is limited to about

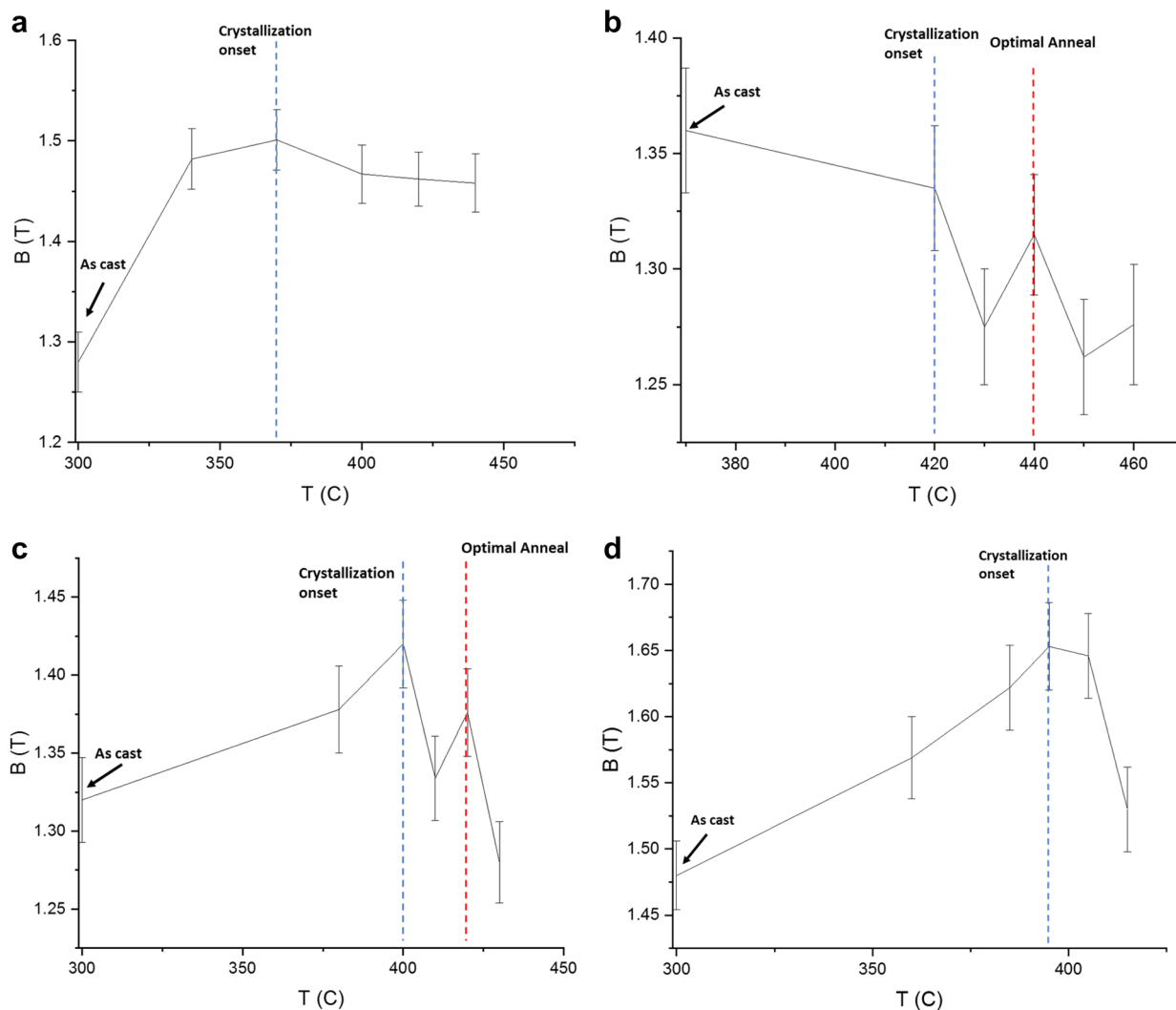
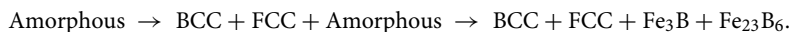


Figure 6: Saturation induction of (a) $(\text{Fe}_{70}\text{Ni}_{30})_{82}\text{Nb}_1\text{Si}_1\text{B}_{16}$, (b) $(\text{Fe}_{70}\text{Ni}_{30})_{82}\text{Nb}_2\text{Si}_0\text{B}_{16}$, (c) $(\text{Fe}_{70}\text{Ni}_{30})_{82}\text{Nb}_3\text{Si}_0\text{B}_{15}$, and (d) $(\text{Fe}_{70}\text{Ni}_{30})_{85}\text{Nb}_{0.5}\text{Si}_0\text{B}_{14.5}$ alloys vs. annealing temperature.

370 °C and 1.2 T [3]. M vs. T measurement showed an unusually sharp increase in magnetization with crystallization, and polymorphic crystallization was suspected. However, from XRD results, it is evident that crystallization follows a 2-step process:



This is similar to results for the previously developed $(\text{Fe}_{70}\text{Ni}_{30})_{80}$ alloy, where annealing to induce primary crystallization results in a BCC + FCC mixture, with a residual amorphous phase [34]. Although a broad amorphous peak is not seen in XRD results, the presence of a residual amorphous phase is known based on the 2-step crystallization process, and the behavior of other MANC materials [4, 35, 36]. This is also confirmed by the presence of an amorphous halo in the TEM diffraction images. The single-step crystallization seen in the

M vs. T results is the result of the low 1 °C/min heating rate in this experiment. Based on these results, the material may be annealed to induce primary crystallization while avoiding secondary crystallization, which is necessary for soft magnetic

properties. Secondary crystallization forms the 23:6 phase often observed in other MANC alloys [37]. This phase has two distinct crystal structures when formed with metalloids or with early transition metals. This is attribute to the preferences of metalloids in special positions accommodating the smaller atoms and for larger early transition metal atoms to occupy more spatial sites [38].

With annealing, 2 distinct trends emerged in coercivity vs. annealing temperature. $(\text{Fe}_{70}\text{Ni}_{30})_{82}\text{Nb}_2\text{Si}_0\text{B}_{16}$ and

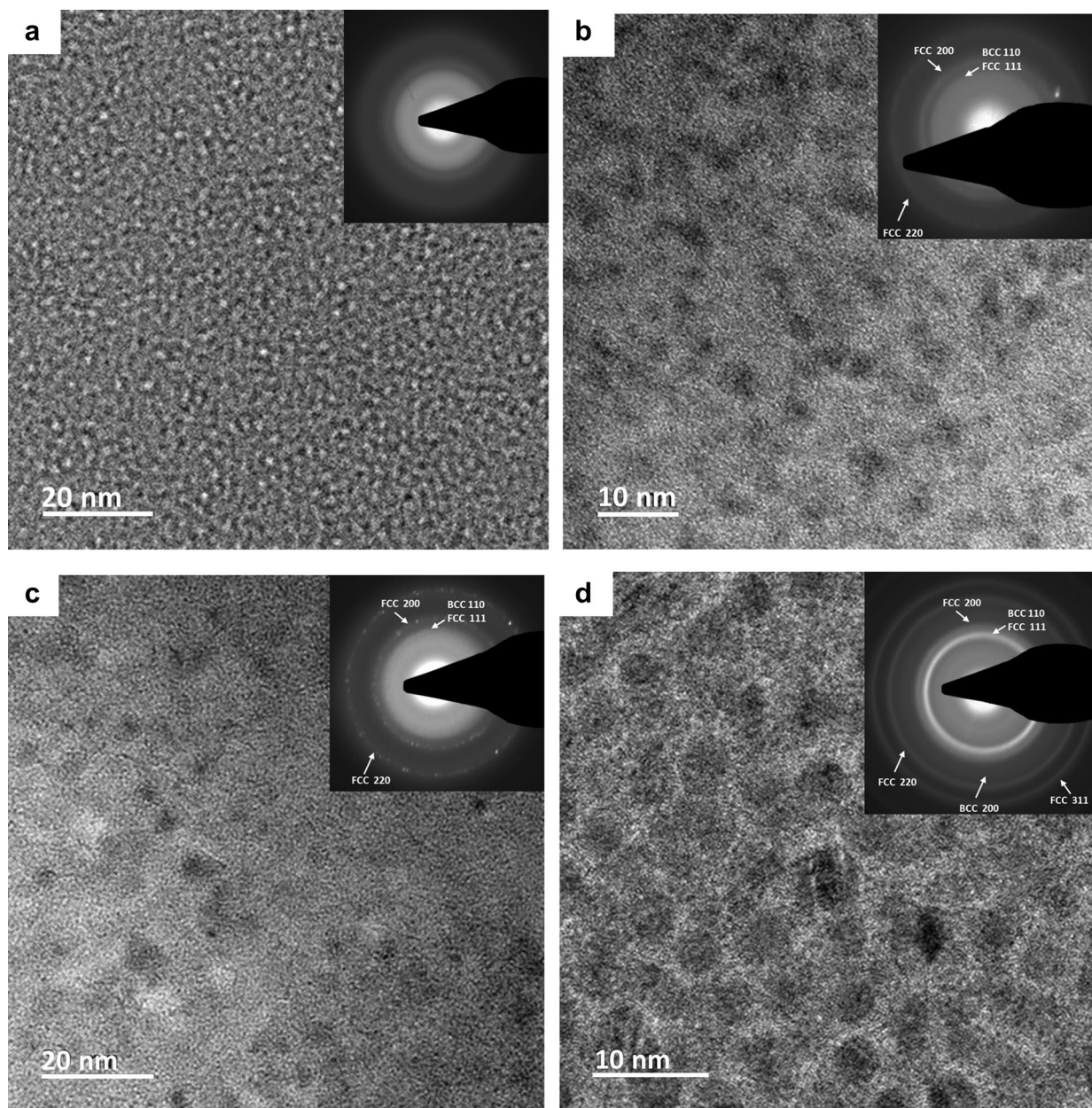


Figure 7: Bright-field TEM images for as-cast (a) $(\text{Fe}_{70}\text{Ni}_{30})_{82}\text{Nb}_1\text{Si}_1\text{B}_{16}$, (b) $(\text{Fe}_{70}\text{Ni}_{30})_{82}\text{Nb}_2\text{Si}_0\text{B}_{16}$, (c) $(\text{Fe}_{70}\text{Ni}_{30})_{82}\text{Nb}_3\text{Si}_0\text{B}_{15}$, and (d) $(\text{Fe}_{70}\text{Ni}_{30})_{85}\text{Nb}_{0.5}\text{Si}_0\text{B}_{14.5}$ alloys.

$(\text{Fe}_{70}\text{Ni}_{30})_{82}\text{Nb}_3\text{Si}_0\text{B}_{15}$ showed sharp drops in coercivity upon crystallization, achieving low coercivities that compare favorably with many existing MANC materials. These two alloys had higher Nb content. $(\text{Fe}_{70}\text{Ni}_{30})_{82}\text{Nb}_1\text{Si}_1\text{B}_{16}$ and $(\text{Fe}_{70}\text{Ni}_{30})_{85}\text{Nb}_{0.5}\text{Si}_0\text{B}_{14.5}$ alloys had lower Nb content, and as a result, coercivity increased to high levels for both of these alloys and remained high after crystallization. The high coercivity can be explained to be the result of excessive crystal coarsening. Nb content in these alloys is only 0.5–1%, which limits its ability to inhibit grain growth. Nb limits grain growth by a process called

soft impingement. The large Nb atoms have low solubility in Fe and Ni crystalline grains and must be rejected to allow crystallization, resulting in a shell of higher Nb content around the grains [34]. Diffusion typically proceeds along a composition gradient, but proximity of other grains results in the overlap of the Nb-enriched shells, resulting in decrease in grain growth by soft impingement [39]. Alloys with low Nb content may not form a sufficient Nb-enriched shell to result in soft impingement. The annealing treatment consisted of 0.5 h at annealing temperature, which gave plenty of time for crystal growth.

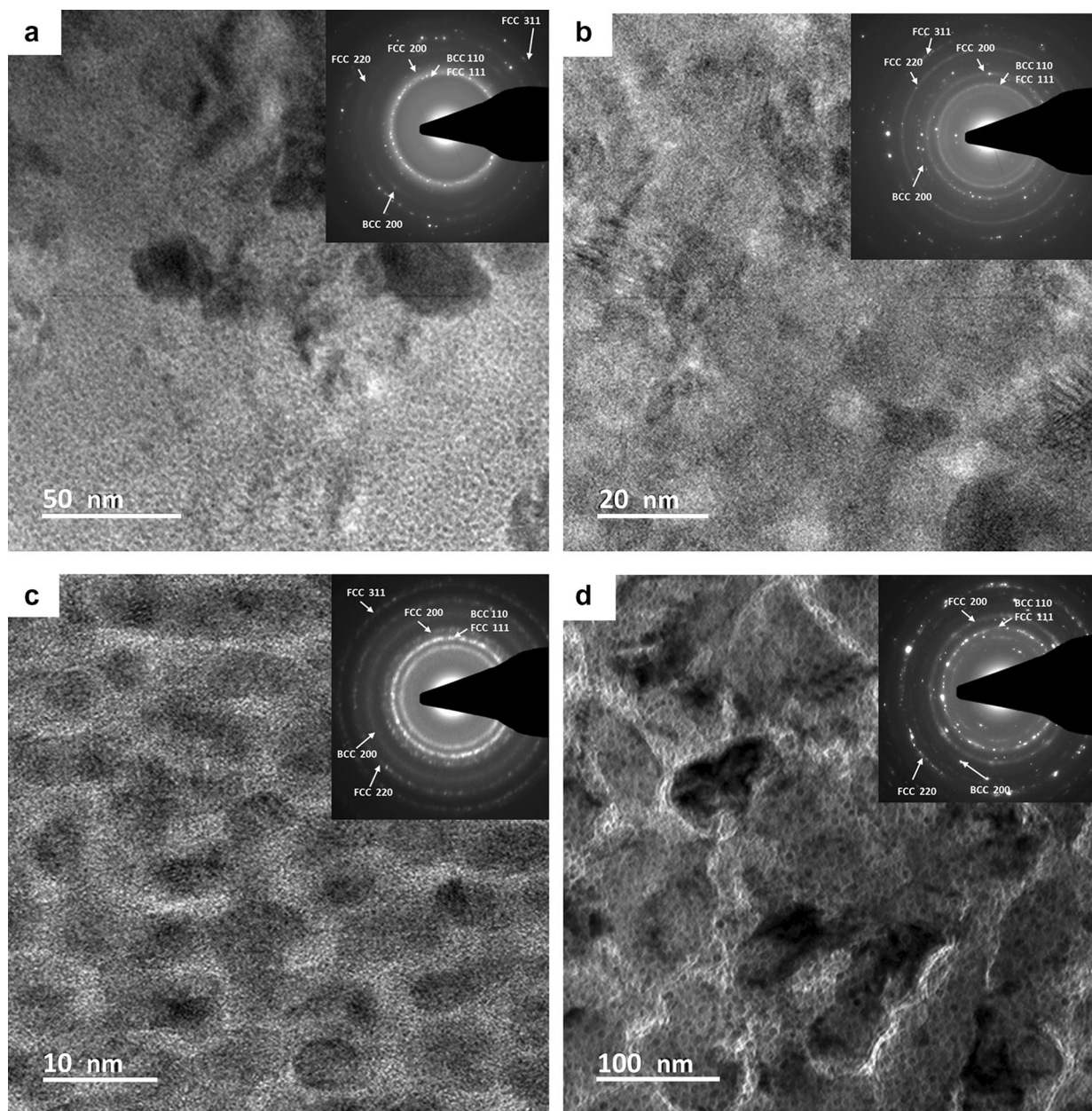


Figure 8: TEM results for annealed (a) $(\text{Fe}_{70}\text{Ni}_{30})_{82}\text{Nb}_1\text{Si}_1\text{B}_{16}$, (b) $(\text{Fe}_{70}\text{Ni}_{30})_{82}\text{Nb}_2\text{Si}_0\text{B}_{16}$, (c) $(\text{Fe}_{70}\text{Ni}_{30})_{82}\text{Nb}_3\text{Si}_0\text{B}_{15}$, and (d) $(\text{Fe}_{70}\text{Ni}_{30})_{85}\text{Nb}_{0.5}\text{Si}_0\text{B}_{14.5}$ alloys.

A rapid annealing treatment, which will allow crystallization to occur without time for excessive grain growth, will be explored in future work. Rapid annealing is a technique that has been explored for nanocrystalline alloys with low or no growth inhibitor content [40]. It has been shown to limit grain size below 20 nm even in alloys that completely dispense with transition metal growth inhibitors such as Nb [35, 41, 42]. Annealing, whether conventional or rapid has the additional advantage of reducing magnetostrictive coupling to residual stress, which lowers losses. This has been shown by Kernion et al. [43] and Takahara et al. [44], and it has been noted that the B-H curve

becomes more square when the magnetostriction coefficient is negative. B-free Fe-based MANCs have also been studied [36]. Such alloys can also have higher inductions as well as lower costs as B is an expensive component both pure and in ferroboron.

TEM results of the annealed samples confirm this explanation. TEM results of the $(\text{Fe}_{70}\text{Ni}_{30})_{82}\text{Nb}_2\text{Si}_0\text{B}_{16}$ and $(\text{Fe}_{70}\text{Ni}_{30})_{82}\text{Nb}_3\text{Si}_0\text{B}_{15}$ alloys show small grains 5–20 nm in diameter, which is ideal for optimal magnetic properties, while the $(\text{Fe}_{70}\text{Ni}_{30})_{82}\text{Nb}_1\text{Si}_1\text{B}_{16}$ and $(\text{Fe}_{70}\text{Ni}_{30})_{85}\text{Nb}_{0.5}\text{Si}_0\text{B}_{14.5}$ alloys had much larger grains, greater than 100 nm in the latter case. TEM results of the as-cast alloys show that only $(\text{Fe}_{70}\text{Ni}_{30})_{82}\text{Nb}_1\text{Si}_1\text{B}_{16}$

was fully amorphous. However, the other 82% alloys had only a small degree of crystallization and were mostly amorphous.

The distribution as well as the exact location relative to the ribbon thickness of the very large grains seen in the thicker parts of the as-cast samples is unknown. They may be biased towards the air side of the ribbon, since cooling rate on the ribbon's air side is lower, giving the material more time to crystallize. These large grains may contribute to coercivity, which is confirmed by the disappearance of these large grains in the annealed alloys with the lowest coercivity. In future work, the alloys will be cast thinner, in the 16–18 μm range, to reduce the presence of these large grains and reduce coercivity in the as-cast state. Cross-sectional TEM will also be performed on both the thicker and thinner cast ribbons to determine the exact distribution of these large grains.

Most interestingly, $(\text{Fe}_{70}\text{Ni}_{30})_{85}\text{Nb}_{0.5}\text{Si}_0\text{B}_{14.5}$ had a nearly ideal structure of sub 10 nm grains with a uniform amorphous matrix surrounding them. The high saturation and moderate coercivity of the as-cast ribbon compare very favorably to other MANC alloys. The formation of this nearly ideal structure in the as-cast state suggests the possibility of producing useful MANC material without requiring subsequent annealing. If coercivity can be reduced by casting thinner ribbon, the combination of magnetic properties and a one-step production process will make this material ideal for large-scale motor applications.

All alloys showed a ΔT_{xg} of 12–23 $^{\circ}\text{C}$, which should allow some thermomechanical forming and stamping operations. A more rapid heating rate will also shift T_{x1} to higher temperatures, allowing a larger formability range. Hot stamping and thermomechanical processing will be explored in future work.

Conclusion

Thermocalc simulations were used to identify compositions with minima in liquidus and solidification range, which have good GFA. This technique was used to identify compositions with good GFA with higher magnetic element content. This resulted in alloys with up to 85% magnetic elements being identified and successfully cast. The alloys showed improvement in Curie temperatures and B_{s} , especially for the $x = 85\%$ alloy. Crystallization for this alloy was shown to proceed in a 2-step process, and an optimal annealing temperature was selected. Annealing studies showed that the $(\text{Fe}_{70}\text{Ni}_{30})_{82}\text{Nb}_2\text{Si}_0\text{B}_{16}$ and $(\text{Fe}_{70}\text{Ni}_{30})_{82}\text{Nb}_3\text{Si}_0\text{B}_{15}$ alloys showed excellent magnetic properties with optimal annealing, with low coercivities and high saturation inductions. TEM studies showed that these alloys had fine grain structure upon annealing, especially the $(\text{Fe}_{70}\text{Ni}_{30})_{82}\text{Nb}_3\text{Si}_0\text{B}_{15}$ alloy. Additionally, the $(\text{Fe}_{70}\text{Ni}_{30})_{85}\text{Nb}_{0.5}\text{Si}_0\text{B}_{14.5}$ alloy had an excellent structure in the as-cast state, with uniform fine grains, raising the possibility that this alloy could be used in the as-cast state.

As-cast saturation induction of this alloy was excellent, at 1.48 T. The coercivity was moderately high, but this was likely due to internal stresses and surface crystallization in the ribbon and can be improved with better casting processes. Future work will explore rapid annealing to limit grain growth, as well as thermo-mechanical processing studies.

Materials and methods

In this study, 3 alloys were produced in the $(\text{Fe}_{70}\text{Ni}_{30})_x(\text{B}-\text{Si}-\text{Nb})_{100-x}$ alloy for $x = 82$, with compositions $(\text{Fe}_{70}\text{Ni}_{30})_{82}\text{Nb}_1\text{Si}_1\text{B}_{16}$, $(\text{Fe}_{70}\text{Ni}_{30})_{82}\text{Nb}_2\text{Si}_0\text{B}_{16}$, and $(\text{Fe}_{70}\text{Ni}_{30})_{82}\text{Nb}_3\text{Si}_0\text{B}_{15}$. An additional alloy was produced at $x = 85$, at $(\text{Fe}_{70}\text{Ni}_{30})_{85}\text{Nb}_{0.5}\text{Si}_0\text{B}_{14.5}$. All alloys were produced by melting 3 times in an Ar atmosphere in a Centorr Vacuum Industries Series 5 furnace, and then melt spinning in an Edmund-Buhler Sc melt spinner. Wheel speed was 35 m/s, and nozzle size was 1 mm. Samples were cut into 0.025–0.035 g pieces and measured in a Perkin Elmer DSC 8500 in an Ar atmosphere to 700 $^{\circ}\text{C}$ at a 40 $^{\circ}\text{C}/\text{min}$ heating rate to determine Curie temperature (T_{c}), T_{g} , and T_{x} . T_{c} measurements were confirmed using a Quantum Design PPMS magnetometer by heating to 800 K at 20 K/s in a 200 Oe field. PPMS measurements were taken of saturation induction as well. Wider ribbon of 3.5 mm was cast using the Edmund-Buhler SC melt spinner with the wheel speed reduced to 31.8 m/s. Samples were annealed at temperatures of 415–445 $^{\circ}\text{C}$ after encapsulation in Ar atmosphere. XRD measurements were taken of these samples to determine crystallization products. Strips of ribbon 150 mm long were annealed in a carbolite furnace and tested on a Laboratorio Elettrofisico Automatic Magnetic Hysteresisgraph for saturation induction and coercivity. 3 mm disks were cut from the as-cast and annealed ribbon and thinned by plasma ion polishing system (PIPS) for TEM. TEM imaging was done on a Tecnai TEM with a 200 kV accelerating voltage.

Acknowledgments

This material is based upon work supported by the U.S. Department of Energy's Office of Energy Efficiency and Renewable Energy (EERE) under the Vehicle Technologies Program Office Award Number DE-EE0008870. This work was also supported by the DOE/EERE—Office of Advanced Manufacturing Program under Award DE-EE0007867. This work was additionally supported by Carpenter Technologies Corporation.

Data availability

Available upon request.

Declarations

Conflict of interest On behalf of all authors, the corresponding author states that there is no conflict of interest.

References

1. P. Waide, C.U. Brunner, 2011. Energy-efficiency policy opportunities for electric motor-driven systems <https://doi.org/10.1787/5kkg52gb9gjd-en>
2. A.M. Leary, P.R. Ohodnicki, M.E. Mchenry, Soft magnetic materials in high-frequency, high-power conversion applications. *JOM*. **64**, 772–781 (2012). <https://doi.org/10.1007/s11837-012-0350-0>
3. N. Aronhime, V. DeGeorge, V. Keylin, P. Ohodnicki, M.E. McHenry, The effects of strain-annealing on tuning permeability and lowering losses in Fe-Ni-based metal amorphous nanocomposites. *JOM*. **69**, 2164–2170 (2017). <https://doi.org/10.1007/s11837-017-2480-x>
4. M.E. McHenry, D.E. Laughlin, Magnetic Properties of Metals and Alloys, in: *Phys. Metall. Fifth Ed.*, Elsevier B.V., 2014: pp. 1881–2008. <https://doi.org/10.1016/B978-0-444-53770-6.00019-8>.
5. I. Škorvánek, R. Gerling, The influence of neutron irradiation on the soft magnetic and mechanical properties of amorphous and nanocrystalline $\text{Fe}_{73.5}\text{Cu}_1\text{Nb}_3\text{Si}_{13.5}\text{B}_9$ alloys. *J. Appl. Phys.* **72**, 3417–3422 (1992). <https://doi.org/10.1063/1.351414>
6. M.A. Willard, F. Johnson, J.H. Claassen, R.M. Stroud, M.E. McHenry, V.G. Harris, Soft magnetic nanocrystalline alloys for high temperature applications. *Mater. Trans.* **43**, 2000–2005 (2002). <https://doi.org/10.2320/matertrans.43.2000>
7. A.M. Leary, V. Keylin, P.R. Ohodnicki, M.E. McHenry, Stress induced anisotropy in CoFeMn soft magnetic nanocomposites. *J. Appl. Phys.* **117**, 1–5 (2015). <https://doi.org/10.1063/1.4919230>
8. T.M. Heil, K.J. Wahl, A.C. Lewis, J.D. Mattison, M.A. Willard, Nanocrystalline soft magnetic ribbons with high relative strain at fracture. *Appl. Phys. Lett.* (2007). <https://doi.org/10.1063/1.2742598>
9. M. Kurniawan, V. Keylin, M.E. McHenry, Effect of alloy substituents on soft magnetic properties and economics of Fe-based and Co-based alloys. *J. Mater. Res.* **30**, 2231–2237 (2015). <https://doi.org/10.1557/jmr.2015.197>
10. M. Kurniawan, V. Keylin, M.E. McHenry, Alloy substituents for cost reduction in soft magnetic materials. *J. Mater. Res.* **30**, 1072–1077 (2015). <https://doi.org/10.1557/jmr.2015.56>
11. N. Aronhime, E. Zoghlin, V. Keylin, X. Jin, P. Ohodnicki, M.E. McHenry, Magnetic properties and crystallization kinetics of $(\text{Fe}_{100-x}\text{Ni}_x)_{80}\text{Nb}_4\text{Si}_2\text{B}_{14}$ metal amorphous nanocomposites. *Scr. Mater.* **142**, 133–137 (2018). <https://doi.org/10.1016/j.scriptamat.2017.08.043>
12. J.M. Silveyra, A. Leary, V. DeGeorge, S. Simizu, M.E. McHenry, High speed electric motors based on high performance novel soft magnets. *J. Appl. Phys.* **115**, 17A319 (2014). <https://doi.org/10.1063/1.4864247>
13. J.M. Silveyra, P. Xu, V. Keylin, V. DeGeorge, A. Leary, M.E. McHenry, Amorphous and nanocomposite materials for energy-efficient electric motors. *J. Electron. Mater.* **45**, 219–225 (2015). <https://doi.org/10.1007/s11664-015-3968-1>
14. A. Urata, H. Matsumoto, S. Sato, A. Makino, High Bs nanocrystalline alloys with high amorphous-forming ability. *J. Appl. Phys.* **105**, 2007–2010 (2009). <https://doi.org/10.1063/1.3072373>
15. C. Wang, A. He, A. Wang, J. Pang, X. Liang, Q. Li, C. Chang, K. Qiu, X. Wang, Effect of P on glass forming ability, magnetic properties and oxidation behavior of FeSiBP amorphous alloys. *Intermetallics* **84**, 142–147 (2017). <https://doi.org/10.1016/j.intermet.2016.12.024>
16. A. Wang, C. Zhao, A. He, H. Men, C. Chang, X. Wang, Composition design of high Bs Fe-based amorphous alloys with good amorphous-forming ability. *J. Alloys Compd.* **656**, 729–734 (2016). <https://doi.org/10.1016/j.jallcom.2015.09.216>
17. T. Liu, A. Wang, C. Zhao, S. Yue, X. Wang, C.T. Liu, Compositional design and crystallization mechanism of high Bs nanocrystalline alloys. *Mater. Res. Bull.* **112**, 323–330 (2019). <https://doi.org/10.1016/j.materresbull.2019.01.007>
18. J. Xu, Y.Z. Yang, W. Li, Z.W. Xie, X.C. Chen, Effect of the substitution of C for Si on microstructure, magnetic properties and bending ductility in high Fe content FeSiBCuPC alloy ribbons. *J. Alloys Compd.* **727**, 610–615 (2017). <https://doi.org/10.1016/j.jallcom.2017.08.181>
19. J. Xu, Y.Z. Yang, W. Li, X.C. Chen, Z.W. Xie, Effect of P addition on glass forming ability and soft magnetic properties of melt-spun FeSiBCuC alloy ribbons. *J. Magn. Magn. Mater.* **417**, 291–293 (2016). <https://doi.org/10.1016/j.jmmm.2016.05.103>
20. E. Dastanpour, M.H. Enayati, A. Masood, V. Ström, On the glass forming ability (GFA), crystallization behavior and soft magnetic properties of nanomet-substituted alloys. *J. Non. Cryst. Solids.* **529**, 119774 (2020). <https://doi.org/10.1016/j.jnoncrysol.2019.119774>
21. X.Y. Yan, Y.A. Chang, Y. Yang, F.Y. Xie, S.L. Chen, F. Zhang, S. Daniel, M.H. He, A thermodynamic approach for predicting the tendency of multicomponent metallic alloys for glass formation. *Intermetallics* **9**, 535–538 (2001). [https://doi.org/10.1016/S0966-9795\(01\)00036-X](https://doi.org/10.1016/S0966-9795(01)00036-X)
22. D. Ma, H. Cao, L. Ding, Y.A. Chang, K.C. Hsieh, Y. Pan, Bulkier glass formability enhanced by minor alloying additions. *Appl. Phys. Lett.* **87**, 1–3 (2005). <https://doi.org/10.1063/1.2115074>
23. H. Cao, D. Ma, K.C. Hsieh, L. Ding, W.G. Stratton, P.M. Voyles, Y. Pan, M. Cai, J.T. Dickinson, Y.A. Chang, Computational thermodynamics to identify Zr-Ti-Ni-Cu-Al alloys with high

- glass-forming ability. *Acta Mater.* **54**, 2975–2982 (2006). <https://doi.org/10.1016/j.actamat.2006.02.051>
24. F. Zhang, C. Zhang, D. Lv, J. Zhu, W. Cao, S. Chen, R. Schmid-Fetzer, Prediction of glass forming ability through high throughput calculation. *J. Phase Equilib. Diffus.* **39**, 562–570 (2018). <https://doi.org/10.1007/s11669-018-0643-2>
 25. Y. Krimer, N. Aronhime, P. Ohodnicki, M.E. McHenry, Prediction of good glass forming ability in amorphous soft magnetic alloys by thermocalc simulation with experimental validation. *J. Alloys Compd.* **814**, 152294 (2020). <https://doi.org/10.1016/j.jallcom.2019.152294>
 26. Z.P. Lu, C.T. Liu, A new glass-forming ability criterion for bulk metallic glasses. *Acta Mater.* **50**, 3501–3512 (2002). [https://doi.org/10.1016/S1359-6454\(02\)00166-0](https://doi.org/10.1016/S1359-6454(02)00166-0)
 27. C.A. Schuh, T.C. Hufnagel, U. Ramamurty, Mechanical behavior of amorphous alloys. *Acta Mater.* **55**, 4067–4109 (2007). <https://doi.org/10.1016/j.actamat.2007.01.052>
 28. J. Lu, G. Ravichandran, W.L. Johnson, Deformation behavior of the $Zr_{41.2}Ti_{13.8}Cu_{12.5}Ni_{10}Be_{22.5}$ bulk metallic glass over a wide range of strain-rates and temperatures. *Acta Mater.* **51**, 3429–3443 (2003). [https://doi.org/10.1016/S1359-6454\(03\)00164-2](https://doi.org/10.1016/S1359-6454(03)00164-2)
 29. N.J. DeCristofaro, P.J. Stamatis, G.E. Fish, Bulk amorphous metal magnetic components for electric motors, US6462456 B1, 2002. [https://doi.org/10.1016/j.\(73\)](https://doi.org/10.1016/j.(73)).
 30. T. Fukao, A. Chiba, M. Matsui, Test results on a super-high-speed amorphous-iron reluctance motor. *IEEE Trans. Ind. Appl.* **25**, 119–125 (1989). <https://doi.org/10.1109/28.18881>
 31. N. Nishiyama, K. Tanimoto, A. Makino, Outstanding efficiency in energy conversion for electric motors constructed by nanocrystalline soft magnetic alloy “nANOMET” cores. *AIP Adv.* **6**, 5 (2016). <https://doi.org/10.1063/1.4944341>
 32. T. Gheiratmand, H.R.M. Hosseini, Finemet nanocrystalline soft magnetic alloy: investigation of glass forming ability, crystallization mechanism, production techniques, magnetic softness and the effect of replacing the main constituents by other elements. *J. Magn. Magn. Mater.* **408**, 177–192 (2016). <https://doi.org/10.1016/j.jmmm.2016.02.057>
 33. N. Aronhime, P. Ohodnicki, M.E. McHenry, Virtual bound states elements and their effects on magnetic and electrical properties of Fe-Ni based metal amorphous nanocomposites. *Scr. Mater.* **169**, 9–13 (2019). <https://doi.org/10.1016/j.scriptamat.2019.05.003>
 34. P. Ohodnicki, E.J. Kautz, A. Devaraj, Y. Yu, N. Aronhime, Y. Krimer, M.E. McHenry, A. Leary, Nanostructure and compositional segregation of soft magnetic FeNi-based nanocomposites with multiple nanocrystalline phases. *J. Mater Res* (2020). <https://doi.org/10.1557/jmr.2020.242>
 35. Z. Li, R. Parsons, B. Zang, H. Kishimoto, T. Shoji, A. Kato, J. Karel, K. Suzuki, Dramatic grain refinement and magnetic softening induced by Ni addition in Fe[B] based nanocrystalline soft magnetic alloys. *Scr. Mater.* **181**, 82–85 (2020). <https://doi.org/10.1016/j.scriptamat.2020.02.020>
 36. P.R. Ohodnicki, S.Y. Park, H.K. McWilliams, K. Ramos, D.E. Laughlin, M.E. McHenry, Phase evolution during crystallization of nanocomposite alloys with Co: Fe ratios in the two-phase region of the binary Fe-Co phase diagram. *J. Appl. Phys.* **101**, 1–3 (2007). <https://doi.org/10.1063/1.2711283>
 37. J. Long, P.R. Ohodnicki, D.E. Laughlin, M.E. McHenry, T. Ohkubo, K. Hono, Structural studies of secondary crystallization products of the Fe₂₃B₆-type in a nanocrystalline FeCoB-based alloy. *J. Appl. Phys.* **101**, 2007–2009 (2007). <https://doi.org/10.1063/1.2714250>
 38. P.R. Ohodnicki, N.C. Cates, D.E. Laughlin, M.E. McHenry, M. Widom, Ab initio theoretical study of magnetization and phase stability of the (Fe Co, Ni)₂₃B₆ and (Fe Co, Ni)₂₃Zr₆ structures of Cr₂₃C₆ and Mn₂₃Th₆ prototypes. *Phys. Rev. B* **78**, 1–13 (2008). <https://doi.org/10.1103/PhysRevB.78.144414>
 39. T. Pradell, D. Crespo, N. Clavaguera, M.T. Clavaguera-Mora, Diffusion controlled grain growth in primary crystallization: Avrami exponents revisited. *J. Phys. Condens. Matter.* **10**, 3833–3844 (1998). <https://doi.org/10.1088/0953-8984/10/17/014>
 40. R. Parsons, B. Zang, K. Onodera, H. Kishimoto, A. Kato, K. Suzuki, Soft magnetic properties of rapidly-annealed nanocrystalline Fe-Nb-B-(Cu) alloys. *J. Alloys Compd.* **723**, 408–417 (2017). <https://doi.org/10.1016/j.jallcom.2017.06.208>
 41. K. Suzuki, R. Parsons, B. Zang, K. Onodera, H. Kishimoto, A. Kato, Copper-free nanocrystalline soft magnetic materials with high saturation magnetization comparable to that of Si steel. *Appl. Phys. Lett.* **110**, 6–10 (2017). <https://doi.org/10.1063/1.4973772>
 42. K. Suzuki, R. Parsons, B. Zang, K. Onodera, H. Kishimoto, T. Shoji, A. Kato, Nano-crystallization of amorphous alloys by ultra-rapid annealing: an effective approach to magnetic softening. *J. Alloys Compd.* **735**, 613–618 (2018). <https://doi.org/10.1016/j.jallcom.2017.11.110>
 43. S.J. Kernion, M.S. Lucas, J. Horwath, Z. Turgut, E. Michel, V. Keylin, J.F. Huth, A.M. Leary, S. Shen, M.E. McHenry, Reduced losses in rolled Fe_{73.5}Si_{15.5}Nb₃B₇Cu₁ nanocrystalline ribbon. *J. Appl. Phys.* **113**, 15–18 (2013). <https://doi.org/10.1063/1.4794131>
 44. Y. Takahara, H. Matsuda, Change in Magnetic Properties with Annealing of a Cold Rolled Amorphous Fe₇₉B₁₆Si₅ Alloy. *Mater. Trans. JIM.* **35**, 435–438 (1994)